

Disturbance Dynamics in Transitional and Turbulent Flows

C.E. Grosch

Old Dominion University, Norfolk, Virginia 23529

Abstract

The dynamics of an ensemble of linear disturbances with a known probability distribution associated with the initial mode amplitudes are studied in boundary-layer flows through an analysis of the transport equations for the mean disturbance kinetic energy and disturbance energy dissipation rate. Effects of adverse and favorable pressure-gradients on the disturbance dynamics are also included in the analysis. Unlike the fully turbulent regime where nonlinear phase scrambling of the fluctuations affects the flow field in proximity to the wall, the laminar regime fluctuations studied here are influenced across the boundary layer by the solid boundary. In addition to the low Reynolds number, early stage transition regime, the dynamics of these disturbance fields can be related in some respects to the near-wall dynamics of the fully turbulent regime.

1 Introduction

A current challenge in the prediction of wall-bounded turbulent flow fields within the realm of single-point closures is the inability to consistently predict the (upstream) transitioning flow field dynamics. While such transition models exist in the literature, (Dhawan and Narasimha, 1958; Solomon, *et al*, 1995; Steelant and Dick, 1996; Warren and Hassan, 1998), their development has been based more from empirical grounds rather than from first principles. As such, their range of applicability is confined to flows containing the same dynamic features as the “calibration flows” the models were designed for.

In order to develop a general linkage between the transitioning laminar flow and the turbulent flow in a developing boundary layer, for example, it is necessary to have a common mathematical framework from which the disturbances in both regimes can be described. In previous studies (Thacker, Grosch and Gatski, 1999a and 1999b) such a framework was developed by coupling a deterministic description of the evolution of disturbances in the laminar regime with an analysis of an ensemble of such disturbances. The approach is based on the observation that, even in the laminar regime, every flow is subject to an inevitable uncertainty in initial conditions. Therefore, although each individual disturbance evolves deterministically, a probability distribution must be introduced for the calculation of ensemble mean properties. This approach is similar to rapid distortion theory (RDT) in that it is based on linearized disturbance equations; however, the realm of application is different. The probability distribution associated with the each initial disturbance mode is given and from that a statistical database of such a distribution of disturbances is developed. These previous studies of disturbance dynamics focused on homogeneous flows (Thacker, *et al*, 1999a), shear flow (Thacker, *et al*, 1999b) in order to develop the methodology and to form a linkage with corresponding turbulent boundary free flows.

The mathematical methodology developed previously is extended to a spatially developing boundary layer with zero, adverse and favorable pressure gradients. The (mean) boundary-layer flow in all cases is extracted from the Falkner-Skan family of solutions, and the disturbance field is a superposition of three-dimensional disturbance modes that are solutions of the Orr-Sommerfeld and Squire equations. A probability distribution that is Gaussian in spanwise wave number and uniform in frequency, describing a white noise spectrum, is assigned to the initial mode amplitudes and used to calculate various correlations such as the ensemble mean disturbance kinetic energy and dissipation rate. With this disturbance database, an analysis of the corresponding kinetic energy and dissipation rate transport equations can be performed and closure models developed for higher-order disturbance field correlations.

2 Analysis

At the outset, a flat, solid-walled boundary located in the (x^*, z^*) plane at $y^* = 0$ is considered (* variables are dimensional quantities). The incompressible flow analysis focuses downstream away from any leading edge effects. Linear disturbance fields are generated which are deviations from an ensemble-mean boundary-layer velocity field given by the Falkner-Skan family of solutions

applicable to flow fields with zero, adverse and favorable pressure gradients. Standard boundary layer scaling is used so that the U_∞^* is the velocity scale, and $L^* = [(2 - \beta) \nu x^* / U_\infty^*]^{1/2}$ is the length scale. The effects of pressure gradient are introduced through the parameter β : $\beta = 0$, zero pressure gradient; $\beta < 0$, adverse pressure gradient; $\beta > 0$, favorable pressure gradient.

The three-dimensional, laminar disturbance modes under consideration are bounded solutions of the linearized Navier-Stokes equations. These velocity and pressure disturbance modes can be written as

$$\begin{bmatrix} \hat{u}_i(y, k_3, \omega, Re) \\ \hat{p}(y, k_3, \omega, Re) \end{bmatrix} e^{i(\mathbf{k} \cdot \mathbf{x} - \omega t)} \quad (1)$$

where $Re (= U_\infty^* L^* / \nu)$ is the Reynolds number based on streamwise location, $\mathbf{k}(Re, \omega) = (k_1(Re, \omega, k_3), 0, k_3)$ is the wave vector in coordinate directions (x, y, z) associated with the most unstable mode, with k_1 complex and k_3 real, and ω is the (real) frequency. These modes are the solutions of the continuity and momentum equations given by

$$ik_1 \hat{u}_1 + \frac{d\hat{u}_2}{dy} + ik_3 \hat{u}_3 = 0 \quad (2)$$

$$(-i\omega + ik_1 U) \hat{u}_1 + \left(\frac{dU}{dy} \right) \hat{u}_2 = -ik_1 \hat{p} + \frac{1}{Re} [\mathcal{L}\hat{u}_1] \quad (3)$$

$$(-i\omega + ik_1 U) \hat{u}_2 = -\frac{d\hat{p}}{dy} + \frac{1}{Re} [\mathcal{L}\hat{u}_2] \quad (4)$$

$$(-i\omega + ik_1 U) \hat{u}_3 = -ik_3 \hat{p} + \frac{1}{Re} [\mathcal{L}\hat{u}_3] \quad (5)$$

with

$$\mathcal{L} = \frac{d^2}{dy^2} - (k_1^2 + k_3^2) = \frac{d^2}{dy^2} - \mathcal{K}^2 \quad (6)$$

where U is the streamwise velocity. These equations are combined to obtain, first the Orr-Sommerfeld equation for the wall normal velocity component \hat{u}_2 with complex eigenvalue k_1

$$\mathcal{L}^2 \hat{u}_2 = iRe(k_1 U - \omega) \mathcal{L}\hat{u}_2 - ik_1 Re \left(\frac{d^2 U}{dy^2} \right) \hat{u}_2 \quad (7)$$

and second, the Squire equation for the normal component of vorticity,

$$\hat{\zeta}_2 = ik_3 \hat{u}_1 - ik_1 \hat{u}_3. \quad (8)$$

$$\frac{d^2 \hat{\zeta}_2}{dy^2} + [iRe(\omega - k_1 U) - \mathcal{K}^2] \hat{\zeta}_2 = ik_3 Re \left(\frac{dU}{dy} \right) \hat{u}_2 \quad (9)$$

Equations (7) and (9) are solved subject to the boundary conditions $\hat{u}_2 = (d\hat{u}_2/dy) = 0$, $\hat{\zeta}_2 = 0$ at $y = 0$, and $\hat{u}_2 \rightarrow 0$, $\hat{\zeta}_2 \rightarrow 0$ as $y \rightarrow \infty$. The Orr-Sommerfeld equation is solved using the compound matrix algorithm employing a fourth order Runge-Kutta integrator combined with an iteration on the eigenvalue. Once the eigenvalue, k_1 , and eigenfunction, \hat{u}_2 , are found, the Squire equation can be solved for $\hat{\zeta}_2$. The Squire equation is quite stiff so it is solved by an implicit method; the second derivative is approximated by a fourth order stencil and the

resulting penta-diagonal system is solved by a generalized Thomas algorithm. With \hat{u}_2 and $\hat{\zeta}_2$ known, Eqs. (2) and (8) are solved simultaneously for \hat{u}_1 and \hat{u}_3 . Finally, with the velocity field $\hat{\mathbf{u}}$ known, the pressure is found from (3).

The velocity and pressure disturbance fields can be constructed from these disturbance mode solutions by considering an ensemble of linear superpositions of modes with initial mode amplitudes $\Phi(\omega, k_3)$ so that

$$u_i(\mathbf{x}, t) = \int d\omega dk_3 \Phi(\omega, k_3) \hat{u}_i(y, \omega, k_3) e^{i(\int k_1 dx + k_3 z - \omega t)} \quad (10)$$

$$p(\mathbf{x}, t) = \int d\omega dk_3 \Phi(\omega, k_3) \hat{p}(y, \omega, k_3) e^{i(\int k_1 dx + k_3 z - \omega t)} \quad (11)$$

This ensemble is described by a probability distribution of $\Phi(\omega, k_3)$ so that its mean, $\langle \Phi(\omega, k_3) \rangle$ is zero, and its covariance is homogeneous (z -direction) and stationary,

$$\langle \Phi^*(\omega, k_3) \Phi(\omega', k'_3) \rangle = \delta(\omega - \omega') \delta(k_3 - k'_3) \mathcal{P}(\omega, k_3). \quad (12)$$

In addition, the probability density $\mathcal{P}(\omega, k_3)$ is partitioned as

$$\mathcal{P}(\omega, k_3) = \mathcal{P}(\omega) \mathcal{P}(k_3) \quad (13)$$

with

$$\mathcal{P}(k_3) = \sqrt{\frac{a}{\pi}} e^{-ak_3^2} \quad (14)$$

$$(15)$$

$$\mathcal{P}(\omega) = \begin{cases} \frac{1}{\omega_H - \omega_L} & \omega_L < \omega < \omega_H \\ 0 & \text{otherwise} \end{cases} \quad (16)$$

The probability density associated with the wavenumber k_3 assumes a Gaussian form with $\sqrt{2a}$ the mean spanwise extent of the initial disturbance field. The probability density associated with frequency assumes a flat (white noise) spectrum where ω_L and ω_H are chosen to encompass the region of disturbance growth computed from linear stability theory.

3 Results

Figure 1 shows the growth rate contours obtained from the linear stability analysis for the zero pressure gradient case. The disturbance field with $k_3 = 0$ is a two component, (u_1, u_2) , two dimensional, *i.e.* independent of x_3 , field. With $k_3 > 0$ the disturbance flow field is a three component, three dimensional, one. The wider the range of values of k_3 the more three dimensional the flow. However, from these plots of the growth rate contours one sees that the modes with the larger values of k_3 have, at any Re , a smaller range of unstable frequencies and a smaller maximum growth rate as compared to the range and maximum growth rate of modes with $k_3 = 0$.

It is now possible to easily form the second-moment correlations from the disturbance velocity and pressure fields given in Eqs. (10) and (11). For example, the disturbance stress tensor is given by

$$\begin{aligned}\tau_{ij}(x, y) &= \langle u_i^* u_j + u_i u_j^* \rangle \\ &= \frac{1}{2} \int d\omega dk_3 \mathcal{P}(\omega, k_3) e^{-2 \int \text{Im}(k_1) dx} (\hat{u}_i^* \hat{u}_j + \hat{u}_i \hat{u}_j^*),\end{aligned}\quad (17)$$

and the disturbance isotropic dissipation rate is given by

$$\begin{aligned}\varepsilon(x, y) &= \frac{1}{Re} \left\langle \frac{\partial u_j}{\partial x_k} \frac{\partial u_j^*}{\partial x_k} \right\rangle \\ &= \frac{1}{Re} \int d\omega dk_3 \mathcal{P}(\omega, k_3) e^{-2 \int \text{Im}(k_1) dx} \\ &\quad \times \left[(|k_1|^2 + k_3^2) \hat{u}_j^* \hat{u}_j + \frac{d\hat{u}_j^*}{dy} \frac{d\hat{u}_j}{dy} \right]\end{aligned}\quad (18)$$

Figures 2 and 3 show the variation of the total disturbance kinetic energy, K , and isotropic dissipation rate, ε , as a function of streamwise distance from the initial position where the disturbance field was generated. Initially (small $x - x_0$) K decreases because the flow is stable at the initial position but thereafter at locations where the mean flow is unstable the kinetic energy grows rapidly with increasing streamwise distance. At x_0 the dissipation rate, ε , is quite large. Similarly to the behavior of K , ε decays initially but at a much greater rate than the decay of K . The minimum in ε coincides with the downstream location where $K = 1$ and thereafter ε grows with increasing x . Despite the growth of ε , it is clear that the production of K outweighs the dissipation because there is overall growth in the kinetic energy.

Figures 4, 5, and 6 show the variation of the scaled disturbance kinetic energy and isotropic dissipation rate across the boundary layer at different streamwise locations. As shown the variables are in terms of wall units such that $K^+ = K^*/(u_\tau^*)^2$, $\varepsilon^+ = \varepsilon^*/((u_\tau^*)^4/\nu^*)$ and $y^+ = y^* u_\tau^*/\nu^*$. with the friction velocity determined from $u_\tau^* = \sqrt{\tau_{12}^*|_w}$ where τ_{12}^* is that of the mean flow, i.e. $\tau_{12}^* = dU^*/dy^*$. Scaling with u_τ^* is straightforward. The mean profile, $U(y)$, is obtained from the solution of Falkner-Skan equation with pressure gradient parameter β , $y = y^*/L^*$ and $U = U^*/U_\infty^*$. From the definitions

$$\left(\frac{u_\tau^*}{U_\infty^*} \right)^2 = \left(\frac{\nu^*}{U_\infty^* L^*} \right) \left(\frac{dU}{dy} \right)_{y=0} = \left(\frac{S_0}{Re} \right) \quad (19)$$

and

$$y^+ = \left(\frac{y^* u_\tau^*}{\nu^*} \right) = \left(\frac{y^*}{L^*} \right) \left(\frac{U_\infty^* L^*}{\nu^*} \right) \left(\frac{S_0}{Re} \right)^{1/2} = (S_0 Re)^{1/2} y \quad (20)$$

with both S_0 and Re functions of β .

Figure 4 shows that shape of the kinetic energy distribution in y^+ is approximately the same at each downstream location with only the peak values growing in the region where the boundary

layer is unstable. Also, as shown in Figure 4, the majority of the kinetic energy is contained within the inner region of the boundary layer, with $y^+ \leq 80$, independently of the downstream location. The results shown in Figures 5 and 6 show that the dissipation rate is maximum at the wall. This occurs because the disturbance flow field velocity gradients are maximum at the wall. In fact, as can be seen from Figure 5, almost all of the dissipation occurs where y^+ is less than 2 or 3. As the energy increases with increasing downstream distance so does the magnitude of ϵ at the wall. Figure 6 shows the distribution of ϵ with y^+ across the boundary layer. Outside of the immediate neighborhood of the wall the distribution of ϵ with y^+ up to about $y^+ = 50$ is nearly constant and independent of streamwise position. These results suggest that the distribution of K and ϵ with y^+ approximately scale with the total value of the kinetic energy at all of these locations.

Another useful variable to examine, that is directly derivable from Eq. 17, is the anisotropy tensor b_{ij} ,

$$b_{ij} = \frac{\tau_{ij}}{2K} - \frac{\delta_{ij}}{3}. \quad (21)$$

Because the mean flow is a two component, two dimensional flow the symmetry imposed on the disturbance velocity field requires that $b_{13} = b_{23} = 0$. Also, the trace of the anisotropy tensor must vanish. In these calculations all components of the anisotropy tensor and its trace are computed and it is found that b_{13} , b_{23} and the trace are zero to within machine error.

Figures 7 and 8 show the variation of two of the components of the anisotropy tensor b_{ij} across the boundary layer at different streamwise locations. In the inner region, $y^+ \leq 50$, b_{22} (Figure 8) is close to $-1/3$ because the boundary conditions on u_2 require that *both* u_2 and $\partial u_2 / \partial x_2$ be zero at the wall. Thus, the u_1 and u_3 are the dominant components in this region. Further from the wall, b_{11} , b_{22} and b_{33} (not shown) are all close to zero indicating an equipartition of the kinetic energy among all three of the velocity components. Still further from the wall there is a region in which b_{11} is approximately $-1/3$ showing that u_2 and u_3 are the dominant components in this region. Finally, in the outer reaches of the boundary layer the disturbance flow field has an approximate equipartition of the kinetic energy.

The variation of b_{12} across the boundary layer at different streamwise locations is shown in Figure 9. Note that the production of kinetic energy term in the energy balance is proportional to $-\tau_{12}$ so that negative values of b_{12} indicate production of kinetic energy. At all streamwise locations b_{12} is predominantly negative with very small positive values for $y^+ > 100$. This is as expected from the growth K with downstream distance. Although the magnitude of the peak value of b_{12} decreases slightly with increasing $x - x_0$, the range of y^+ over which it is negative increase so that integral of b_{12} over the boundary layer, a measure of the total production of kinetic energy, increases with increasing $x - x_0$.

4 Summary and Conclusions

This research establishes a unified mathematical framework is found for describing disturbances in both the transitioning and turbulent regimes. The transitioning regime is modeled by an ensemble of deterministic solutions of the linearized Navier-Stokes equations described by a probability distribution that accounts for the uncertainty in disturbance initial (upstream) conditions. This yields an upstream kinetic energy spectrum associated with probability distribution of random mode amplitudes of disturbances calculated from the linearized Navier-Stokes equations. In addition using this methodology, transport equations for the disturbance moments were derived. This methodology as applied to stochastic disturbance field, was used to model the early stage of a transitioning boundary layer. The second-moment disturbance velocity correlations and isotropic, disturbance energy dissipation rate were calculated.

It was found that, in a boundary layer in which the disturbance velocity field was growing, that (1) the majority of the disturbance kinetic energy was confined to an inner layer, $y^+ < 60$; (2) almost all of the energy dissipation occurs at and very close to the wall where the disturbance field is predominantly a two (u_1, u_3) component one; and (3) the production of kinetic energy occurs further from the wall, $50 \leq y^+ \leq 100$, where the disturbance flow field is a three component one and there is near equipartition of the kinetic energy among the components.

Further research will involve the study of the production, transport, and destruction terms in mean disturbance kinetic energy and dissipation rate equations with the view to modeling the complex behavior observed in the results of these calculations.

References

- [1] S. Dhawan and R. Narasimha, "Some properties of boundary layer during the transition from laminar to turbulent flow motion," *J. Fluid Mech.* **3**, 418 (1958).
- [2] W. J. Solomon, G. J. Walker and J. P. Gostelow, "Transition length prediction for flows with rapidly changing pressure gradients," ASME Paper ASME-95-GT-241, International Gas Turbine and Aeroengine Congress & Exposition, Houston, Texas, June 5 - 8 (1995).
- [3] J. Steelant and E. Dick, "Modelling of bypass transition with conditioned Navier-Stokes equations coupled to an intermittency transport equation," *Int. J. Num. Meth. Fluids* **23**, 193 (1996).
- [4] E. S. Warren and H. A. Hassan, "Transition Closure Model for Predicting Transition Onset," *J. Aircraft* **35**, 769 (1998).
- [5] W. D. Thacker, T. B. Gatski and C. E. Grosch, "Analyzing Mean Transport Equations of Turbulence and Linear Disturbances in Decaying Flows," *Phys. Fluids* **11**, 2626 (1999).
- [6] W. D. Thacker, C. E. Grosch and T. B. Gatski, "Modeling the Dynamics of Ensemble-Averaged Linear Disturbances in Homogeneous Shear Flow," *Flow Turbul. Combust.* **63**, 39 (1999).

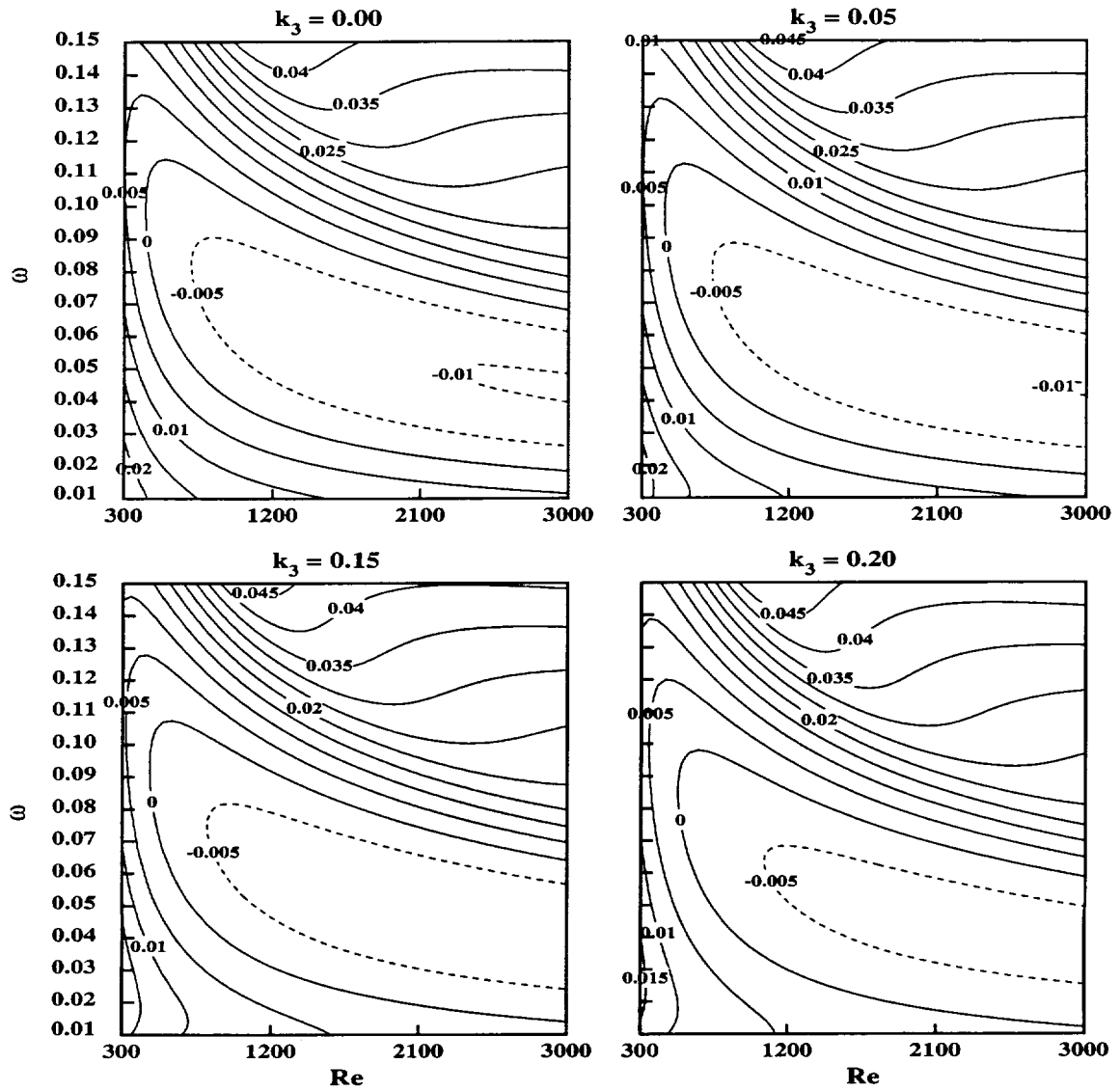


Figure 1: Growth-rate contours $Im(k_1)$ of the zero pressure gradient boundary layer for several values of k_3 , the spanwise wave number.

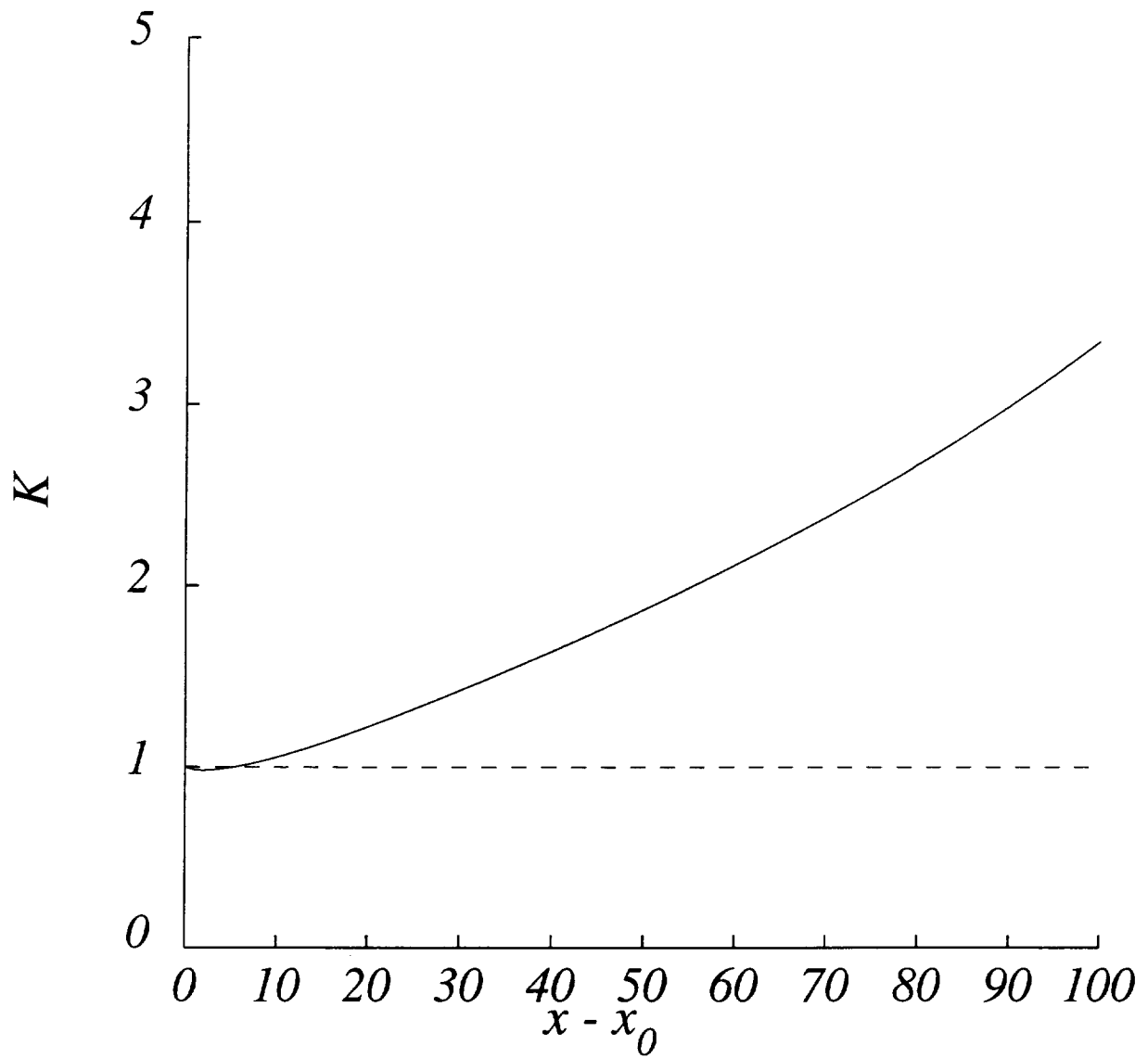


Figure 2: Evolution of the disturbance kinetic energy as a function of the streamwise location.

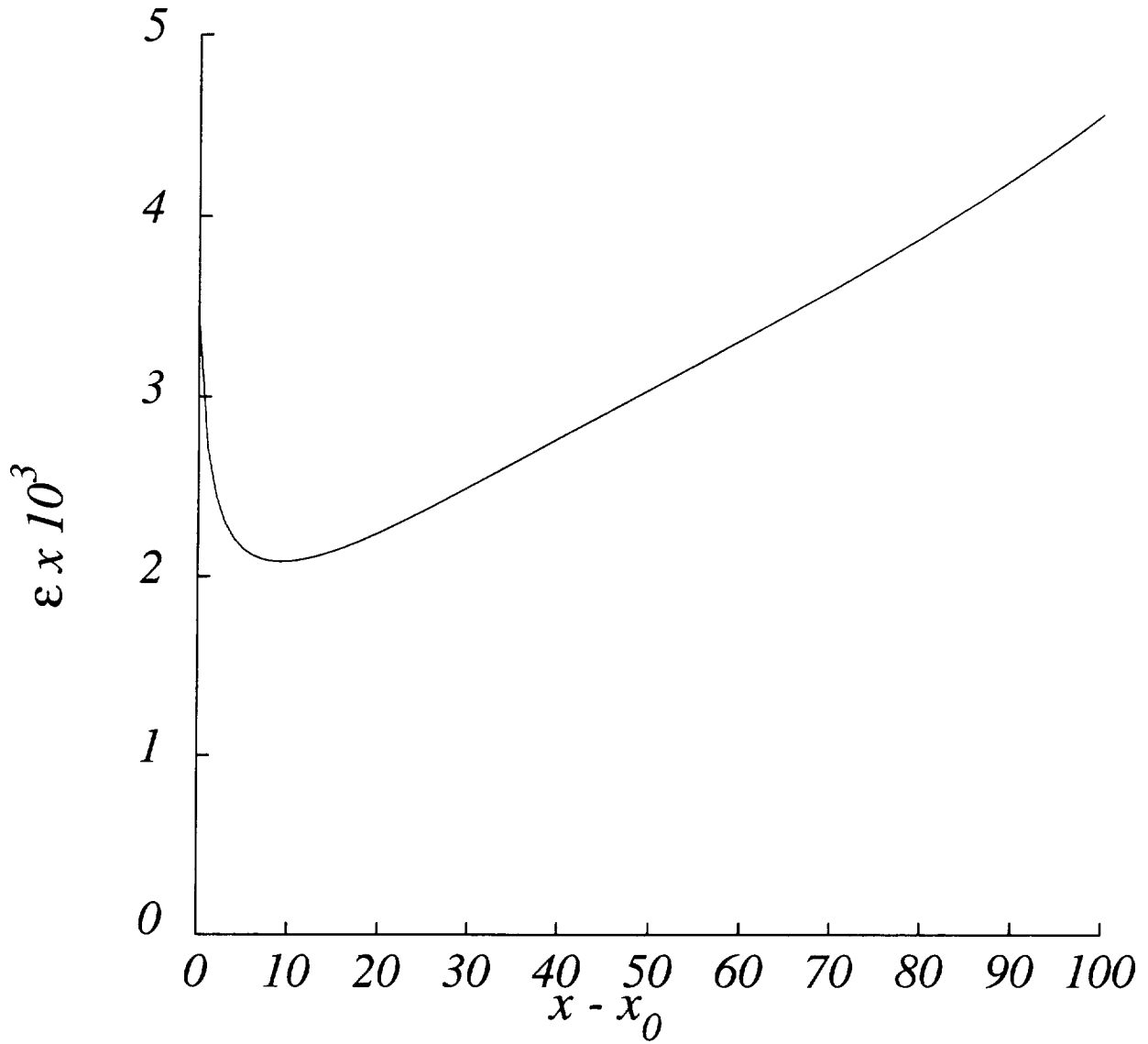


Figure 3: Evolution of the disturbance isotropic dissipation rate as a function of the streamwise location.

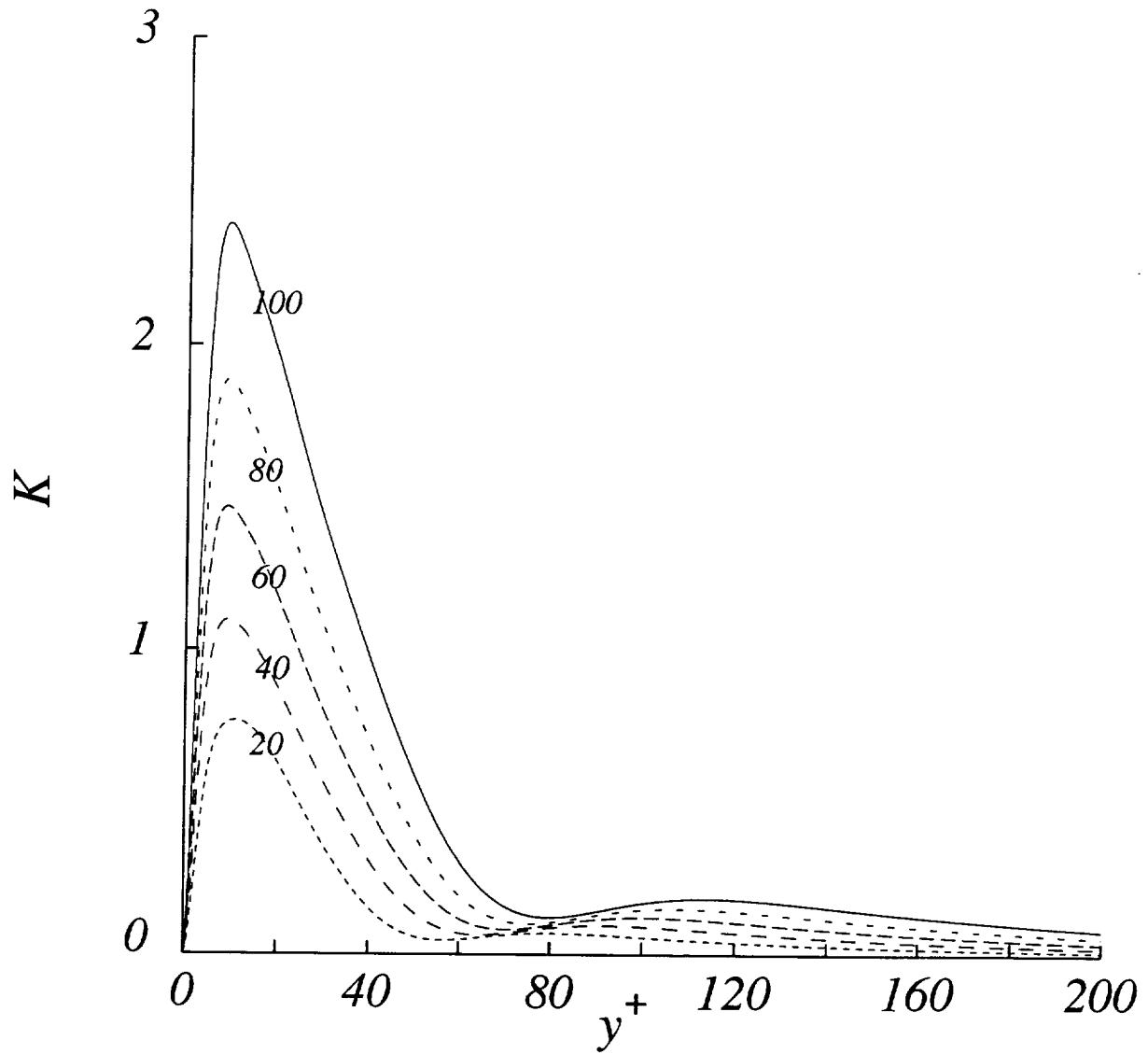


Figure 4: Distribution of the disturbance kinetic energy across boundary layer at various stream-wise locations. The curves are labeled with the values of $x - x_0$.

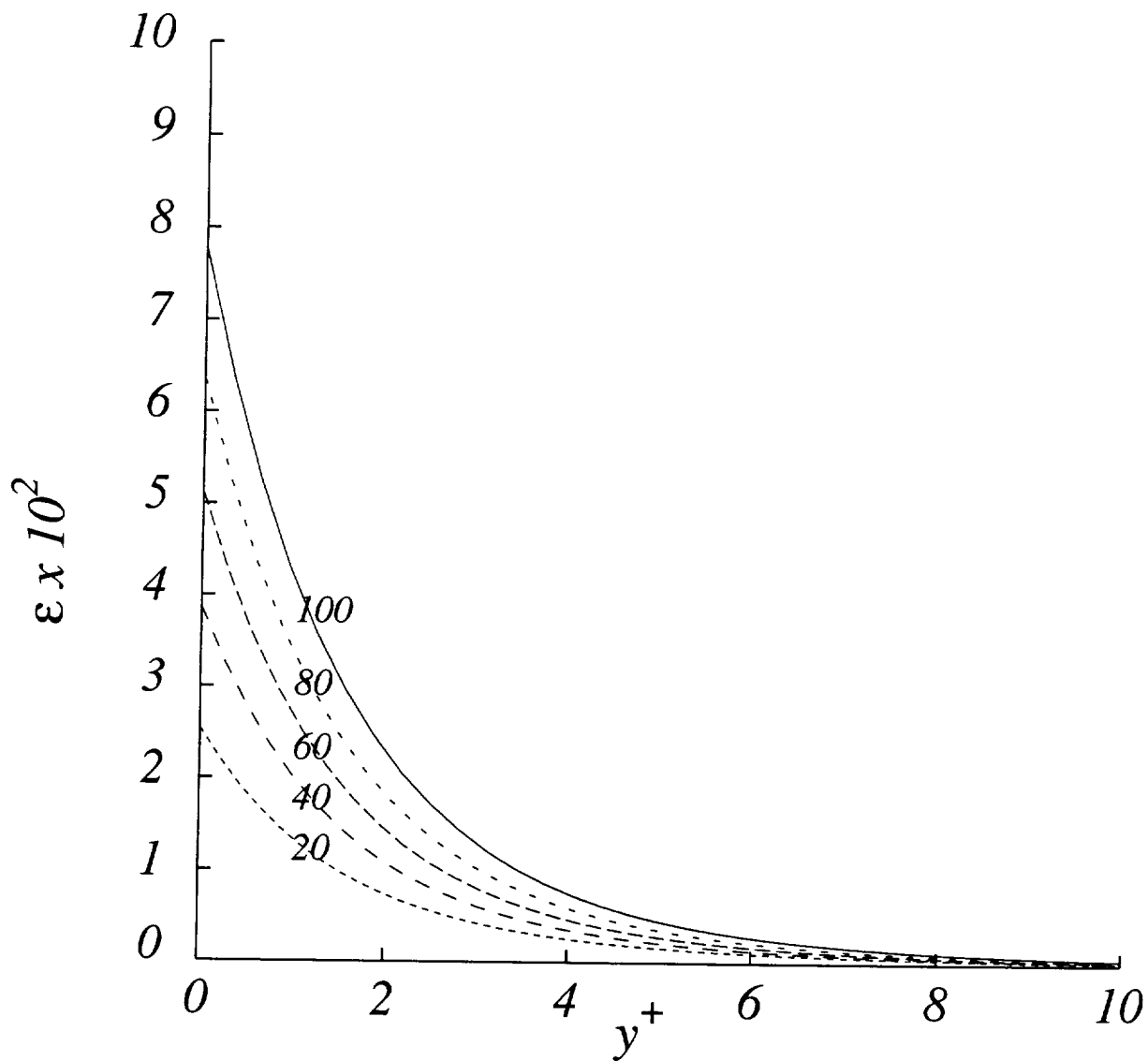


Figure 5: Disturbance isotropic dissipation rate distributions across the inner portion, $y^+ \leq 10$, of the boundary layer at various streamwise locations. The curves are labeled with the values of $x - x_0$.

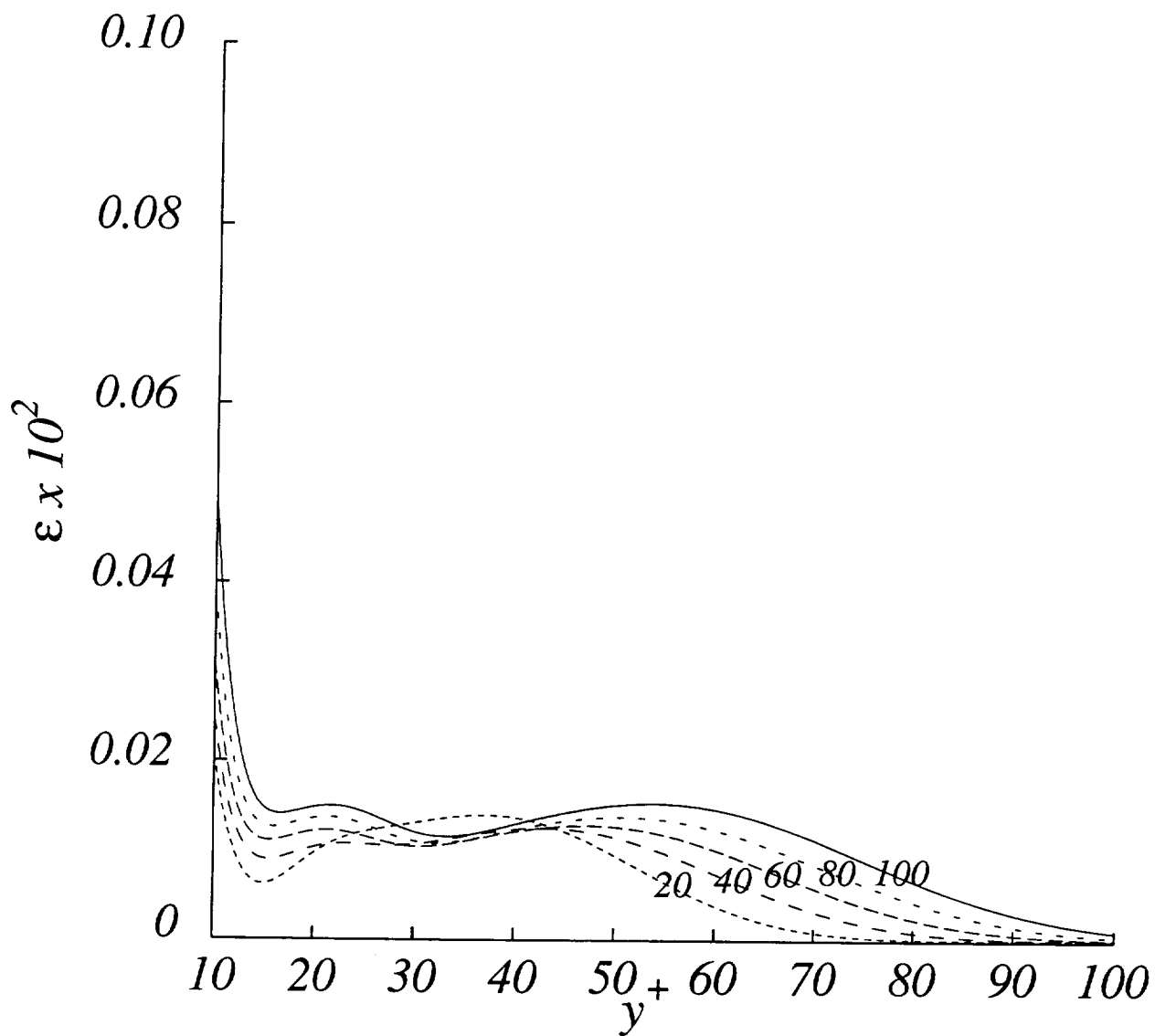


Figure 6: Disturbance isotropic dissipation rate distributions across the boundary layer at various streamwise locations. The curves are labeled with the values of $x - x_0$.

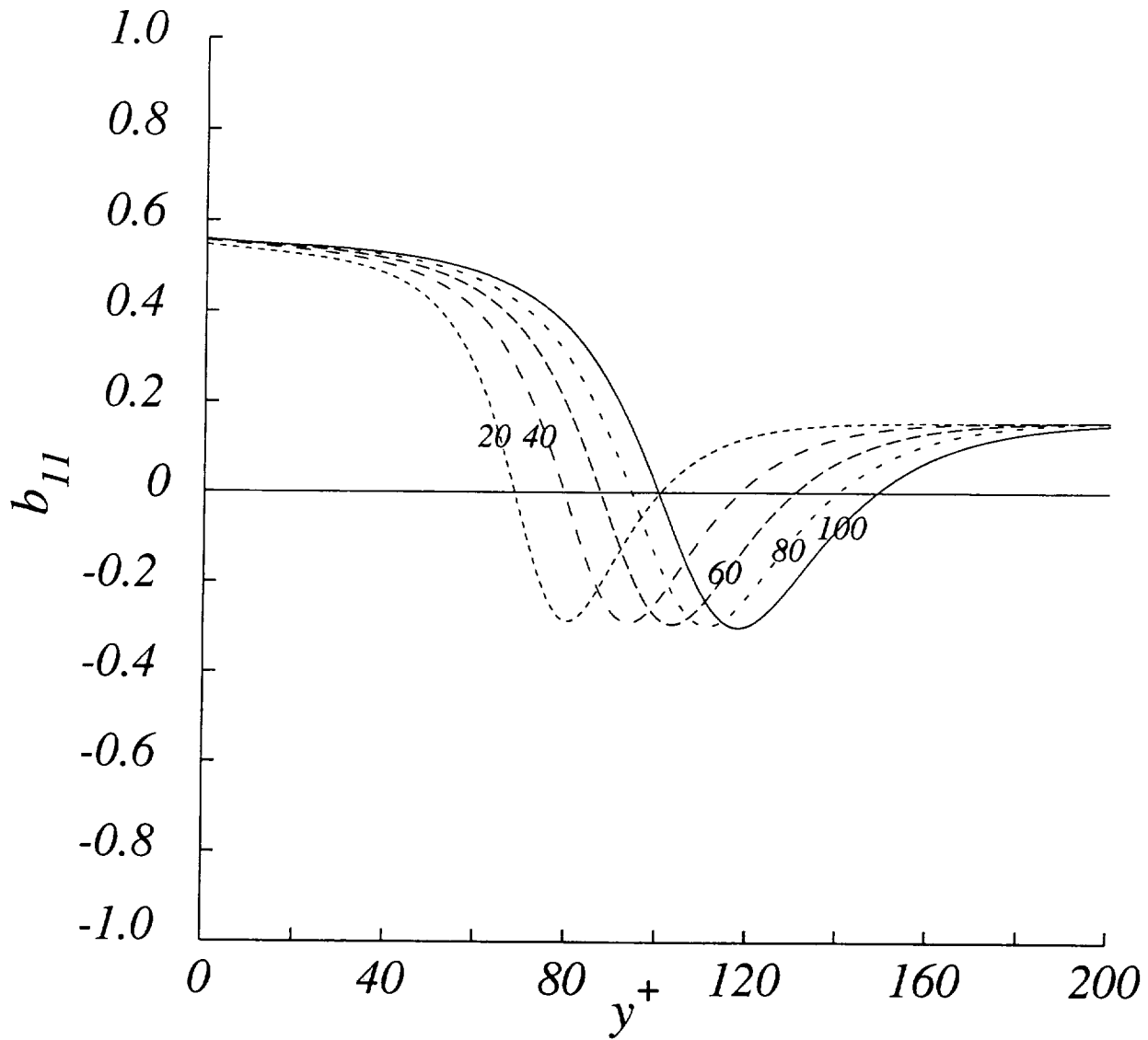


Figure 7: Distribution of b_{11} , one component of the velocity second-moment anisotropy tensor, across the boundary layer at various streamwise locations. The curves are labeled with the values of $x - x_0$.

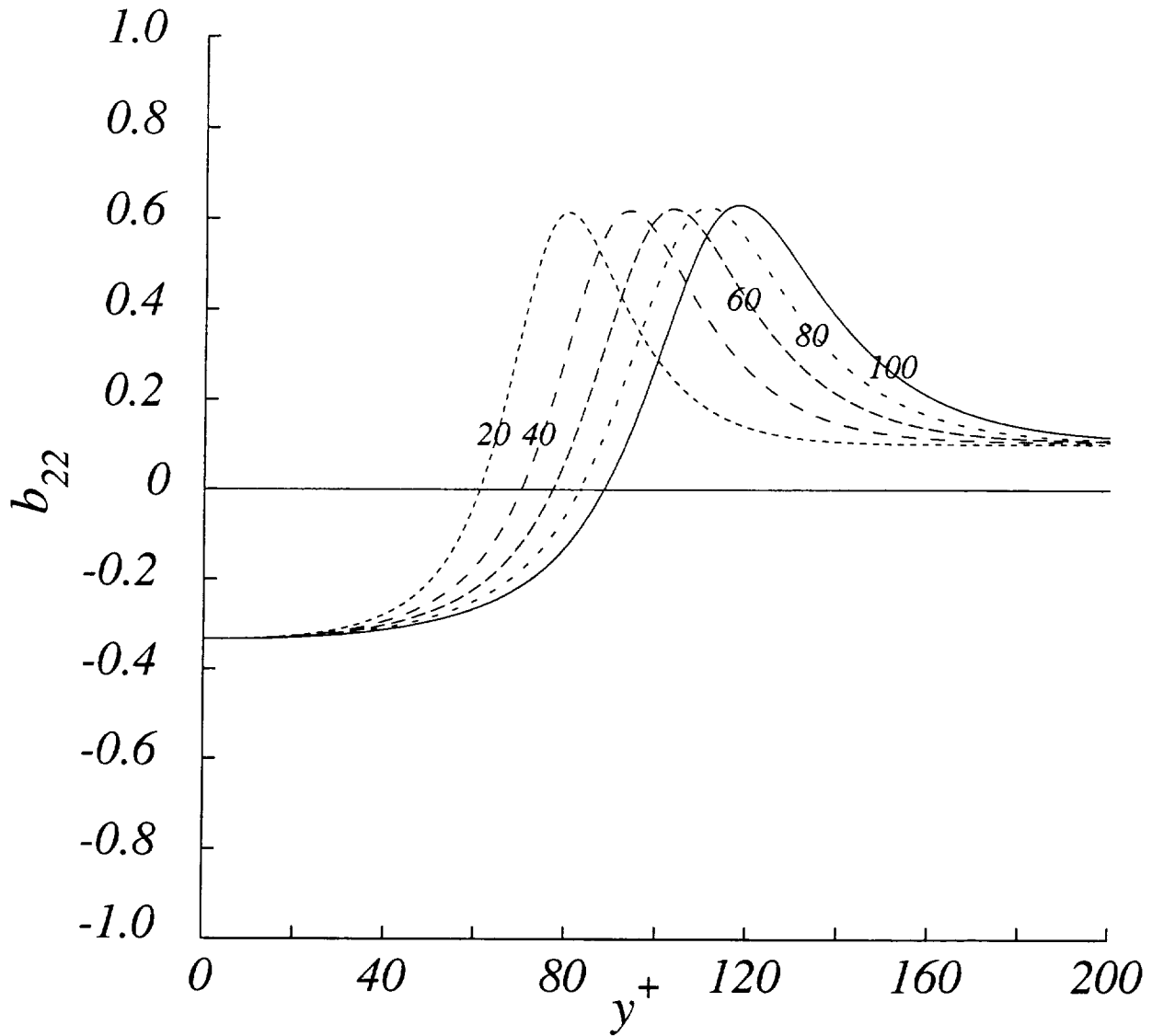


Figure 8: Distribution of b_{22} , one component of the velocity second-moment anisotropy tensor, across the boundary layer at various streamwise locations. The curves are labeled with the values of $x - x_0$.

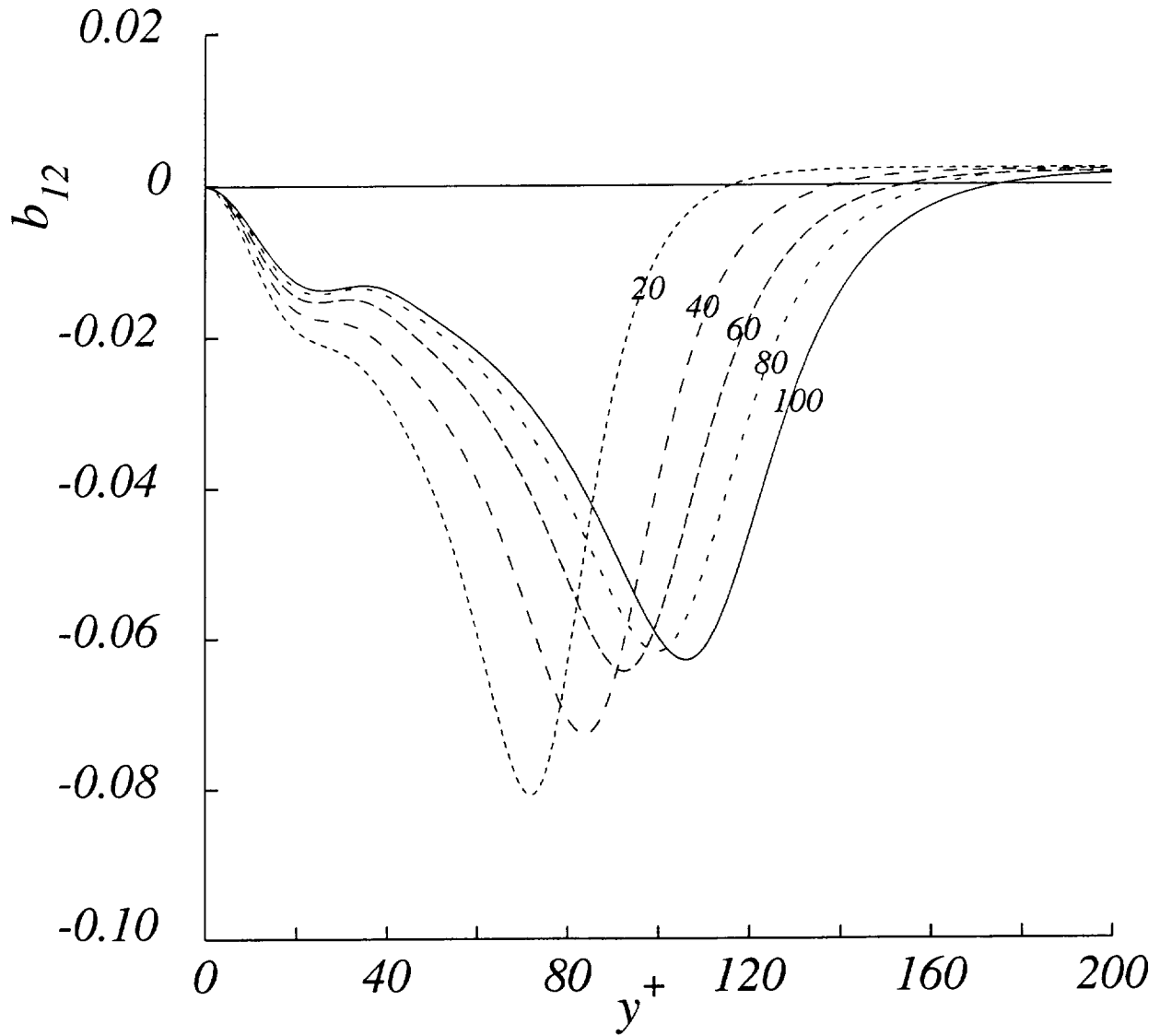


Figure 9: Distribution of b_{12} , one component of the velocity second-moment anisotropy tensor, across the boundary layer at various streamwise locations. The curves are labeled with the values of $x - x_0$.